

1 **The sensitivity of superrotation to the latitude of baroclinic forcing in a**
2 **terrestrial dry dynamical core**

3 Pablo Zurita-Gotor^{a,b} Álvaro Anaya-Benlliure,^a Isaac M. Held^c

4 ^a *Universidad Complutense de Madrid* ^b *Instituto de Geociencia UCM-CSIC* ^c *Princeton*
5 *University*

6 *Corresponding author:* Pablo Zurita-Gotor, pzurita@alum.mit.edu

7 ABSTRACT: Previous studies have shown that Kelvin-Rossby instability is a viable mechanism
8 for producing equatorial superrotation in small and/or slowly rotating planets. It is shown in
9 this paper that this mechanism can also produce superrotation with terrestrial parameters when
10 the baroclinic forcing moves to low latitudes, explaining previous results by Williams. The
11 transition between superrotating and subrotating flow occurs abruptly as the baroclinic forcing
12 moves poleward. Although Kelvin-Rossby instability weakens when the baroclinic zone moves
13 away from the equator, the key factor explaining the abrupt transition is the change in the baroclinic
14 eddies. When differential heating is contained within the tropics, baroclinic eddies do not decelerate
15 the subtropical jet and the upper-tropospheric flow approximately conserves angular momentum,
16 providing conditions favorable for Kelvin-Rossby instability. In contrast, when baroclinic eddies
17 are generated in the extratropics, they decelerate the subtropical jet and prevent the Kelvin-Rossby
18 coupling. Due to this sensitivity to baroclinic eddies the system exhibits hysteresis: near the
19 transition parameter, extratropical eddies can prevent superrotation when they are initially present.

20 1. Introduction

21 Many planetary atmospheres exhibit prograde winds at the equator, a phenomenon known as
22 superrotation. In our solar system, for instance, Venus, Titan, Jupiter and Saturn are all known to
23 superrotate (Read and Lebonnois 2018, and references therein). As tropical-extratropical interac-
24 tions can be fundamentally altered in a superrotating atmosphere (Saravanan 1993), superrotation
25 is often associated with very different climates and feedbacks from the well-known terrestrial
26 climate, and the transition between subrotating and superrotating atmospheres may occur abruptly
27 (Suarez and Duffy 1992). This transition is not beyond the realm of possibility for Earth (Caballero
28 and Huber 2010), so the potential for an abrupt transition is especially of interest.

29 Superrotation implies atmospheric angular momentum locally in excess of that provided by the
30 planet surface, which can only be achieved by means of eddy forcing (Hide 1969). This eddy
31 forcing, however, may have different sources depending on the planet, ranging from thermal tides
32 (Takagi and Matsuda 2007; Mendonça and Read 2016) to convective heating (Schneider and Liu
33 2009) to day-night contrast in tidally-locked planets (Merlis and Schneider 2010; Showman and
34 Polvani 2011). Over the last decade, ageostrophic Kelvin-Rossby instability has emerged as a firm
35 candidate for spinning superrotation in small and/or slowly rotating planets like Venus and Titan.

36 This hypothesis was first suggested by Iga and Matsuda (2005), who found an unstable mixed
37 Kelvin-Rossby mode fluxing momentum into the equatorial region in a shallow-water linear sta-
38 bility analysis of the Venusian atmosphere. Some years later, Mitchell and Vallis (2010) found
39 spontaneous superrotation at large thermal Rossby number in idealized model simulations using
40 the Held and Suarez (1994, HS94 henceforth) model, provided the diabatic forcing of the Hadley
41 cell is not too strong (Dias Pinto and Mitchell 2014). The superrotation in their simulations was
42 driven by a mode with similar characteristics to that described by Iga and Matsuda (2005). A more
43 complete parameter sweep of the HS94 model performed by Potter et al. (2014) confirmed the
44 robustness of superrotation for small/slowly-rotating planets. Wang and Mitchell (2014) extended
45 the linear stability analysis of Iga and Matsuda (2005) to the primitive equations, finding again
46 a mixed Kelvin-Rossby mode that fluxes momentum into the equatorial region with non-small
47 Rossby numbers. More recently, Zurita-Gotor and Held (2018, ZH18 henceforth) have studied the
48 nonlinear equilibration of the instability, finding an irreversible acceleration at the equator as the
49 Kelvin component of the mode steepens and breaks.

50 With the standard forcing and terrestrial parameters, the HS94 model does not superrotate (e.g.
51 Potter et al. 2014) consistent with the small Rossby numbers found on Earth. However, Williams
52 (2003, W03 henceforth) found a transition to superrotation in this model when the radiative-
53 equilibrium baroclinicity moved equatorward. Although Williams attributed the superrotation to
54 barotropic instability, classical barotropic instability cannot produce an acceleration at the equator
55 if the PV gradient is positive at that latitude. It seems more likely that the acceleration found by
56 W03 is due to Kelvin-Rossby instability, as moving the baroclinicity equatorward should favor the
57 interaction between the two waves.

58 Our work is motivated by these results. We will reexamine the simulations of W03 to investigate
59 the role played by Kelvin-Rossby instability for superrotation in that setting at the light of the
60 recent work on the instability described above. Additionally, we will analyze the dynamical
61 factors involved in the transition from subrotating to superrotating climates, which may be relevant
62 for the warm climate superrotation discovered by Caballero and Huber (2010). Moving the
63 baroclinic zone equatorward should not only facilitate Kelvin-Rossby coupling but also weaken
64 baroclinic instability, which Mitchell and Vallis (2010) argued to be important for the transition to
65 superrotation at large thermal Rossby number. Other studies with the dry dynamical core using
66 terrestrial parameters have also found superrotation when the temperature gradient weakens (Laraia
67 and Schneider 2015; Polichtchouk and Cho 2016).

68 **2. Model and forcing**

69 We use in this study the spectral dynamical core of Held and Suarez (1994) based on the source
70 code provided by the University of Exeter (Vallis et al. 2018). The model solves the hydrostatic
71 primitive equations of a dry atmosphere forced by Newtonian cooling and subject to Rayleigh
72 friction over the lower troposphere. Terrestrial values are used for the planet radius and rotation
73 rate.

74 The main modification from the standard HS94 setup is the use of a different radiative equilibrium
75 profile. Williams (2003) showed that this model superrotates when the radiative-equilibrium
76 baroclinicity moves close to the equator. He considered a slightly different radiative-equilibrium

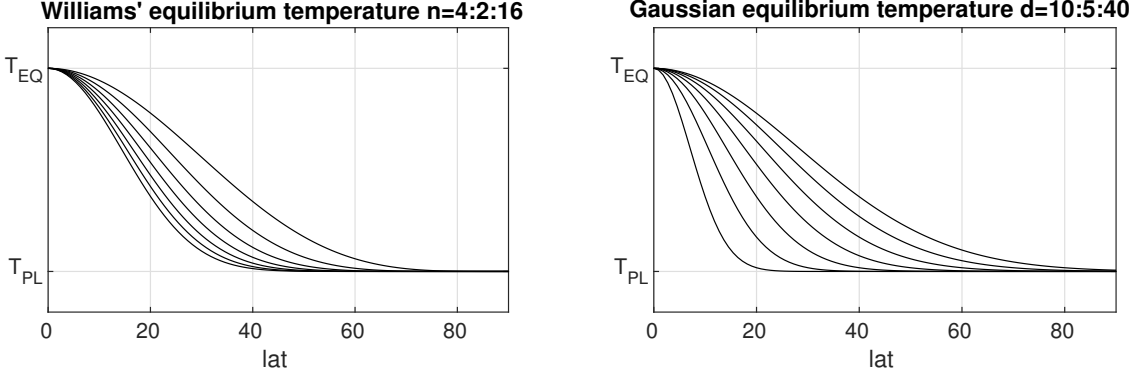


FIG. 1. Radiative-equilibrium meridional temperature structure for (left) the forcing considered by W03 (cf. his Fig. 1), with even values of n ranging from 4 to 16, and (right) the Gaussian forcing described in the text with Gaussian widths ranging from 10 to 40 deg. with 5 deg steps.

formulation from HS94, defined as follows:

$$T_R(\phi, \sigma) = \max \left\{ \sigma^\kappa T_{EQ} \left[1 - \Delta_H (1 - \cos^n \phi) + \Delta_V \frac{1 - \sigma^\kappa}{\kappa} \right], T_{str} \right\} \quad (1)$$

where T_{EQ} and T_{str} are the radiative-equilibrium equatorial surface temperature and stratospheric temperature, respectively, the parameters Δ_H and Δ_V modulate the meridional temperature gradient and static stability, and $\sigma = p/p_s$. The latitudinal structure of the temperature profile is controlled by the even integer n . With increasing n , the temperature gradient steepens and moves towards the equator (Fig. 1, left). Other differences from the standard HS94 setup include a shallower boundary layer depth (200 hPa) and a constant Newtonian timescale ($\tau_R = 20$ days). Although these choices do not affect the model behavior described in this paper, we use the same parameters as W03 to start our analysis in order to replicate his results. Following W03, we take $T_{EQ} = 315K$, $T_{str} = 200K$, and $\Delta_H = \Delta_V = 0.1$.

W03 showed that this model transitions from earth-like to superrotating climates when n increases and the radiative-equilibrium baroclinicity moves equatorward. However, changes in the latitude of maximum baroclinicity are discrete and non-uniform with this formulation, which makes it difficult to study the transition between the two regimes. Thus, we have found it useful to also

95 employ the following alternative forcing formulation:

$$96 \quad T_R(\phi, \sigma) = \max \left\{ \sigma^\kappa T_{EQ} \left[1 - \Delta_H [1 - \exp(-(\phi/d)^2)] + \Delta_V \frac{1 - \sigma^\kappa}{\kappa} \right], T_{str} \right\} \quad (2)$$

97 where the d parameter controls the width of the tropical region, and hence the latitude of maximum
 98 baroclinicity (Fig. 1, right). In contrast with the W03 formulation, this latitude now changes
 99 smoothly with the controlling parameter. We will refer to this formulation as the Gaussian forcing.
 100 In this case, we have chosen parameters more similar to the HS94 setup: an equator-to-pole
 101 temperature difference of $60K$ ($\Delta_H = 0.19$) compared to only $31.5K$ in W03, a boundary layer
 102 depth of 300 hPa and a (uniform) forcing time scale of 40 days. The model behavior described in
 103 this paper is not sensitive to these choices. Although changes in n (with W03's formulation) and
 104 d (with the Gaussian forcing) affect the maximum baroclinicity as well as its location, sensitivity
 105 analyses reveal that it is the latter that is responsible for the results described in this paper.

106 W03 used a rhomboidal truncation R42 with 30 vertical levels equally spaced in σ . The
 107 simulations described in this paper use a T85 resolution with 50 equally spaced levels in σ , but
 108 similar results are obtained using a coarser T42L30 resolution. All simulations are initialized from
 109 an isothermal state. Finally, we note that we include a sponge at the top model level (eddy viscosity
 110 $\nu = 5 \times 10^7 \text{ m}^2/\text{s}$) as in Zurita-Gotor and Held (2021) to reduce artificial reflection.

111 3. Analysis of Williams' results

112 In this section, we revisit the results of W03 to investigate whether the superrotation found by
 113 this author could be due to Kelvin-Rossby instability. We will focus on his $n = 16$ case, but we
 114 have also tried other parameters finding broad agreement with W03.

115 As found by W03, the $n = 16$ simulation superrotates. Fig. 2 (top left) shows the final equilibrium
 116 state: a deep layer of westerlies is observed above 500 hPa at the equator, with maximum values
 117 around 40 m/s near 150 hPa . The lower two panels of Fig. 2 provide some details on the spin up
 118 process by showing time series of zonal wind on the equatorial plane and at the level of maximum
 119 acceleration. We can see that it takes some time for the equatorial westerlies to appear (around day
 120 125), but once they do the acceleration proceeds very rapidly.

126 This delay can be linked to the slow buildup of the subtropical jet on the radiative time scale.
 127 The jet achieves its top speed by day 115 (Fig. 2, top center), at which time the upper-troposphere

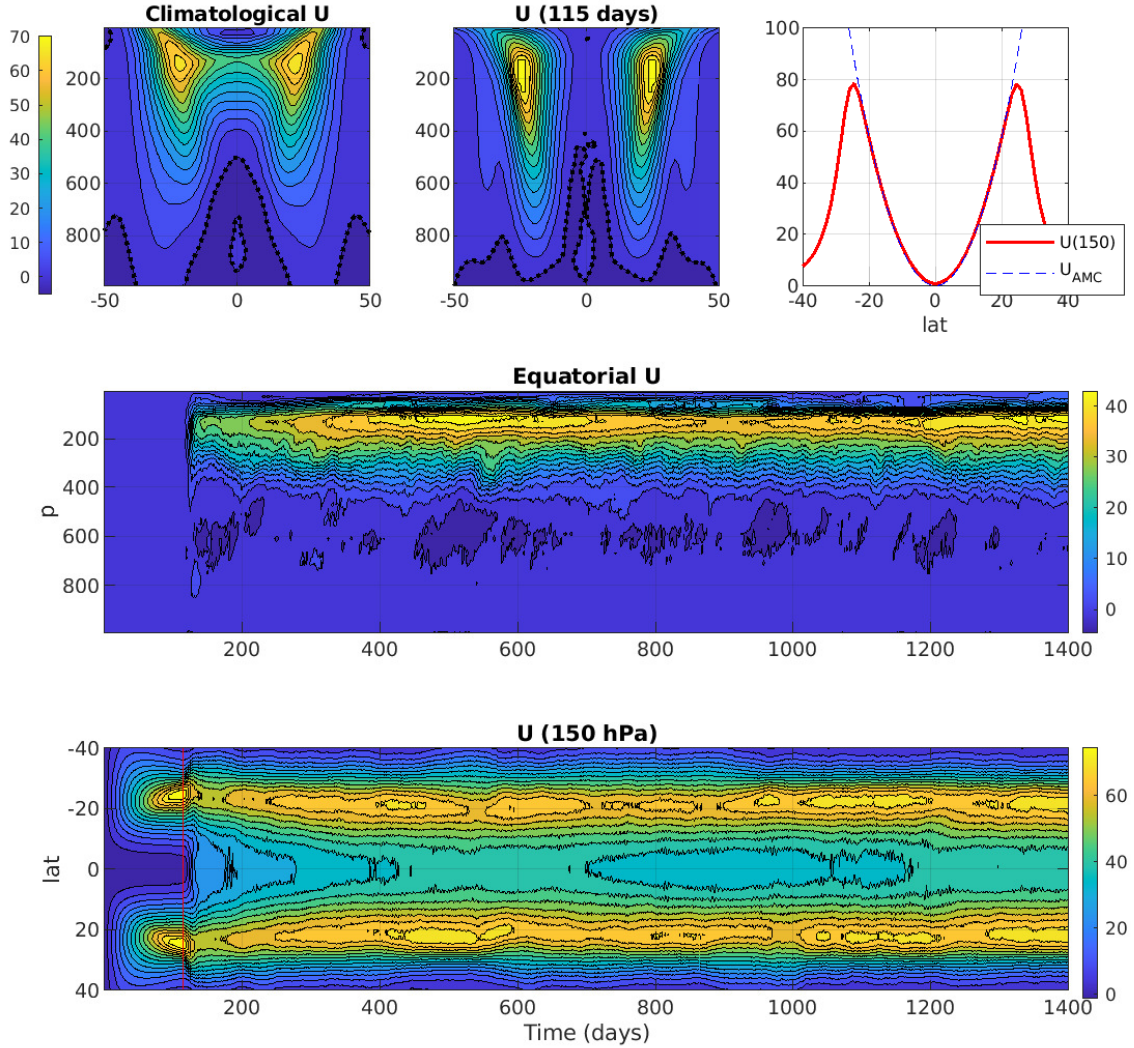


FIG. 2. (top) Equilibrium zonal wind profile (left), zonal wind at $t = 115$ days (center), and the profile at the latter time at 150 hPa (red) compared with the angular-momentum conserving wind in blue dashed line (right). The thick black dotted line on the left two panels shows the zero contour. (middle) Time series of zonal-mean zonal wind on the equatorial plane. (bottom) Time series of zonal-mean zonal wind at 150 hPa. The red line marks the time $t = 115$ days.

flow is very nearly angular-momentum-conserving (Fig. 2, top right). This marks the beginning of the rapid equatorial acceleration (and concomitant deceleration of the subtropical jet), in just a few

130 days. Thereafter, the equatorial acceleration proceeds at a much slower rate, while the subtropical
 131 jet recovers most of its speed. Low-frequency variability is present in the final equilibrated
 132 state (note that Fig. 2 only shows a fraction of the simulation length). A careful inspection of
 133 this variability reveals that the equatorial wind maxima tend to be preceded by the buildup and
 134 equatorward migration of the subtropical jet (and viceversa).

135 To investigate which zonal wavenumbers are responsible for the initial spinup and the inter-
 136 nal zonal wind variability during the equilibrated stage, Fig. 3 shows the timeseries of the
 137 vertically-integrated meridional eddy momentum convergence cospectra at the equator. Following
 138 Zurita-Gotor (2019), we distinguish between the divergent and rotational contributions to the eddy
 139 momentum convergence:

$$140 \quad -\frac{\partial}{\partial y} \left(\overline{u'_r v'_d} + \overline{u'_d v'_r} \right) = \overline{v'_d \xi'} - \overline{u'_r D'} \quad (3a)$$

$$141 \quad -\frac{\partial}{\partial y} \overline{u'_r v'_r} = \overline{v'_r \xi'}, \quad (3b)$$

143 where overbars and primes denote zonal averages and deviations therefrom and the r and d
 144 suscripts denote the rotational and divergent velocity contributions to the horizontal velocity (u, v),
 145 ξ is vertical vorticity and D horizontal divergence. We used a Cartesian expression above for
 146 simplicity (see Zurita-Gotor (2019) for the full spherical expressions including cosine factors).

152 Consistent with previous work (Zurita-Gotor and Held 2018; Zurita-Gotor 2019), the divergent
 153 component (in particular the $\overline{u'_r D'}$ term) is responsible for the equatorial acceleration (Fig. 3, top)
 154 while the rotational eddy momentum fluxes only decelerate the tropics. To capture the full impact
 155 of the latter, we show this term meridionally integrated over the tropics ($|\phi| \leq 20$, Fig. 3 middle)
 156 rather than just at the equator. (The off-equatorial forcing also decelerates the equator by driving
 157 equatorial upwelling).

158 The cospectra show that these two eddy contributions to the equatorial momentum balance are
 159 due to different waves. The divergent acceleration at the equator is due to planetary waves: $k = 2$,
 160 during the initial spinup and a combination of $k = 1 - 3$ during the equilibrated state. In contrast,
 161 the rotational deceleration is due to synoptic eddies ($k = 6 - 7$). The bottom panels of Fig. 3
 162 show the full latitude-pressure structure of the eddy acceleration during the spinup (120-130 days

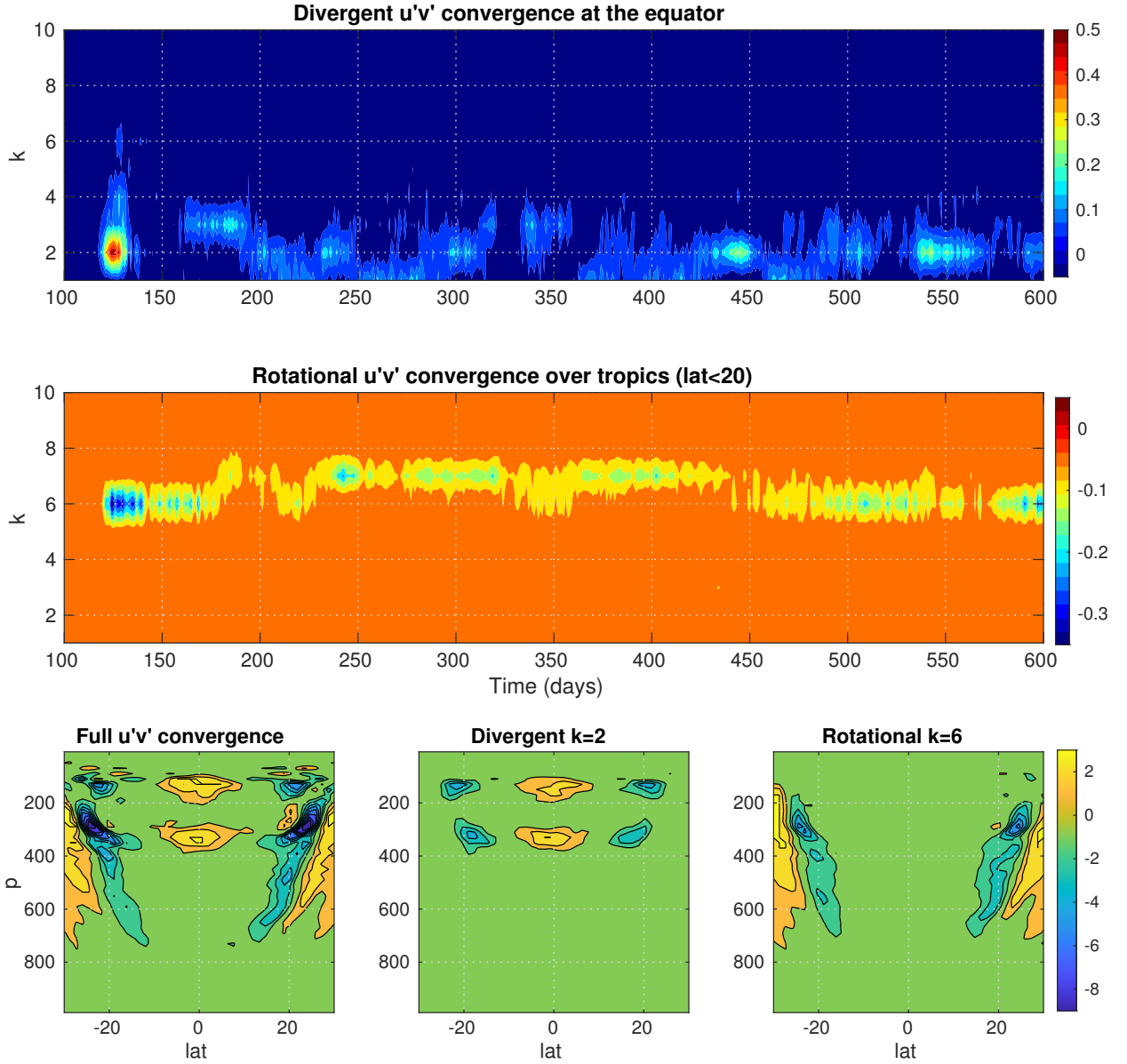


FIG. 3. Cospectra of the vertically-integrated convergence by (top) the divergent eddy momentum flux at the equator, and (middle) the rotational eddy momentum flux averaged over the tropics. Note the reduced time range compared to Fig. 2. (Bottom) Eddy momentum convergence averaged from 120 to 130 days (left), and contributions by (center) the $k = 2$ divergent momentum flux, and (right) the $k = 6$ rotational momentum flux. Accelerations in units of ms^{-1}/day .

average), together with the contributions from the divergent $k = 2$ and rotational $k = 6$ components. These two terms, which have very different structure, capture very well the full eddy acceleration.

165 Kelvin-Rossby instability provides a plausible mechanism to explain W03 superrotation. As
 166 noted by Wang and Mitchell (2014) and ZH18, this instability requires non-small Rossby numbers,
 167 which is typically satisfied in small, slowly-rotating planets but not on Earth. However, in this high-
 168 n simulation in which differential heating remains largely confined within the tropics, the tropical
 169 circulation becomes angular-momentum conserving (implying $Ro = 1$) right before the spinup of
 170 the equatorial westerlies. Kelvin-Rossby growth rates are maximized in this zero-vorticity limit
 171 (ZH18).

172 A linear instability analysis confirms that the angular-momentum-conserving flow observed at
 173 $t = 115$ days supports Kelvin-Rossby instability. The dispersion relation has two peaks (c.f.,
 174 Fig. A1). The maximum growth rates are found for wavenumbers $k = 6, 7$, associated with
 175 baroclinic instability, but a broad peak is also found at small zonal wavenumbers associated with
 176 Kelvin-Rossby modes. See appendix for details.

177 Fig. 4 describes the structure of the $k = 2$ mode responsible for the equatorial acceleration in
 178 the simulation. The mode has maximum amplitudes at the equator and over the subtropical jet.
 179 The subtropical maximum is confined to tropopause levels, while at the equator several maxima
 180 are observed suggestive of vertical propagation. This is reminiscent of the K-R mode described
 181 by ZH18, although the 3D structure is a bit more complicated now, and the meridional phase shift
 182 changes with height. Nevertheless, the horizontal structure at the levels of peak eddy momentum
 183 convergence (130 and 330 hPa) agrees with the characteristic Kelvin-Rossby structure (Wang and
 184 Mitchell 2014), with the subtropical Rossby wave lagging the equatorial Kelvin wave. The Rossby
 185 (Kelvin) component dominates at the upper (lower) $\overline{u'D'}$ maximum.

189 The above analysis provides some evidence in support of the relevance of K-R instability for
 190 the equatorial acceleration. As additional evidence, similar to the simulation described in ZH18
 191 this acceleration is imparted by *vertical* eddy momentum advection occurring in connection with
 192 the steepening and dissipation of the Kelvin wave front. This is illustrated by Fig. 5 (left), which
 193 shows the equatorial potential temperature at the beginning and end of the spinup (days 118 and
 194 130) over the 130-330hPa layer. Vertical eddy momentum advection produces a mean flow forcing
 195 over the same layer (Fig. 5, right), which becomes irreversible when the front is dissipated.

199 We conclude this section with some comments on the maintenance of the equatorial wind in
 200 the equilibrated state. Although it is argued sometimes that K-R instability can spin up but not

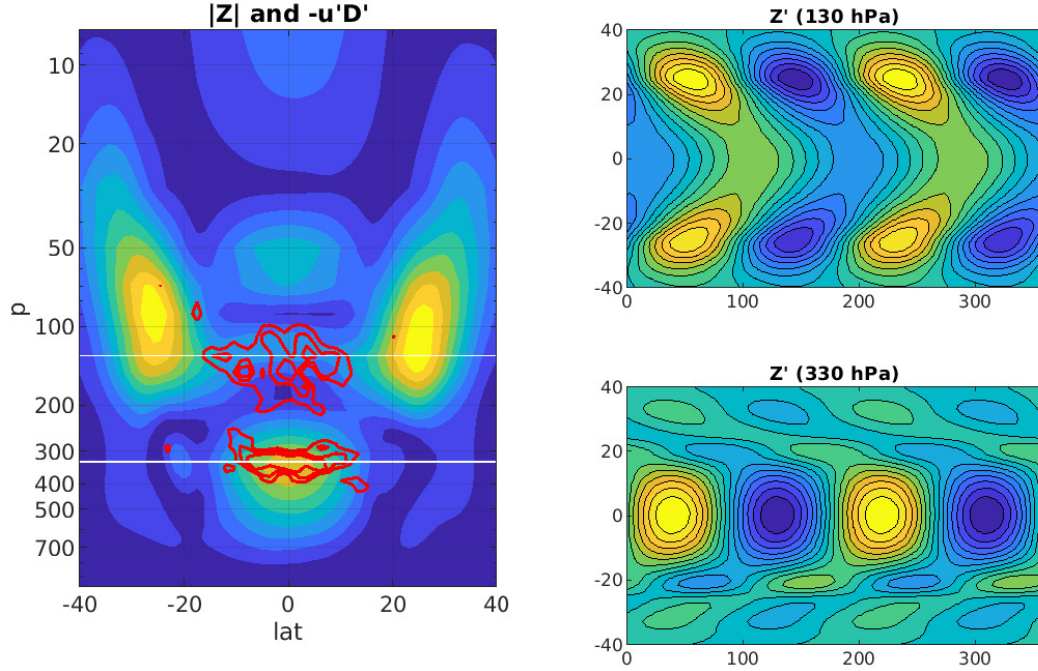


FIG. 4. (left) Amplitude of the $k = 2$ geopotential anomaly (shading) and eddy momentum convergence $-\overline{u'D'}$ (red contours at 1,2,3 ms^{-1}/day) at $t = 125$ days. (right) Horizontal structure of the anomaly at (top) 130 hPa and (bottom) 330 hPa.

maintain superrotation (the Kelvin and Rossby waves cannot propagate at the same phase speed while propagating in opposite directions with respect to the local winds), Fig. 3 (top) shows additional spurts of equatorial acceleration after the initial spinup. However, Fig. 6 (top right) shows that the bulk of this eddy acceleration acts below the levels of maximum equatorial winds. The equatorial jet around 130 hPa can persist because the deceleration is also weak at that level, as the Hadley cell is confined below (Fig. 6, top left).

The equatorial wind variability during the equilibrated regime is driven by the competition between the deceleration by synoptic eddies and the acceleration by planetary waves (Fig. 3). Wavenumber $k = 2$ is again the main contributor to this acceleration, though wavenumbers $k = 1$ and $k = 3$ also play a role. The peak $k = 2$ eddy momentum convergence is found around 330 hPa. At that level, the time-mean absolute vorticity remains very weak (Fig. 6, bottom left), suggesting that

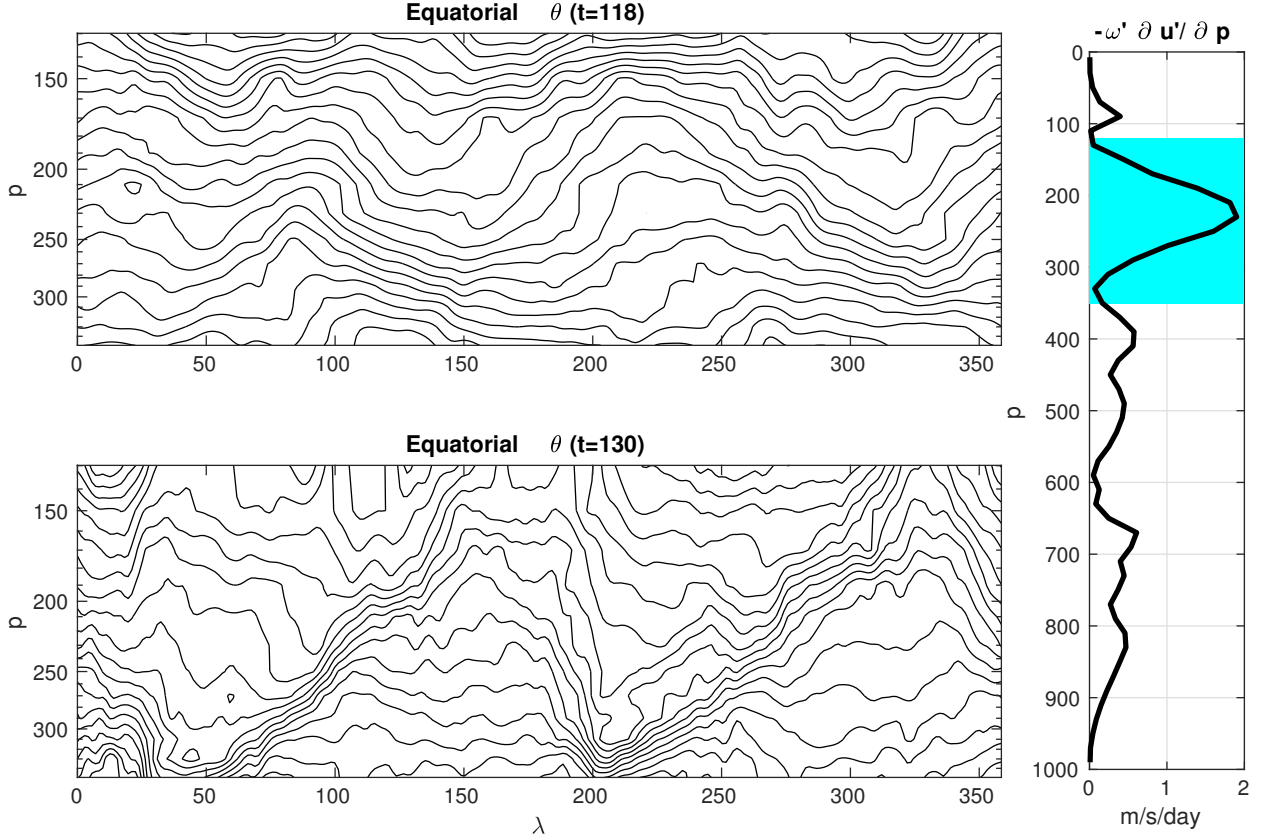


FIG. 5. (left) Equatorial potential temperature over the 330-130 hPa layer at (top) day 118 and (bottom) day 130 of the simulation. (right) Profile of eddy vertical advection at the equator averaged between these two times, with the 330-130 hPa layer shaded.

K-R instability might still be relevant. We have computed a composite of geopotential anomalies for acceleration events exceeding $0.5 \text{ ms}^{-1}/\text{day}$, subject to the additional restrictions of a minimum 5-day duration and a minimum inter-event separation of 20 days. The phase of the geopotential anomalies are homogenized before compositing. The resulting composite anomaly (comprising 52 events) is consistent with coupled Kelvin-Rossby variability (Fig. 6, bottom right).

4. The transition to superrotation

W03 found a transition from subrotating to superrotating climates as n increases, with unsteady behavior at intermediate values of n . To analyze this transition we use the alternative Gaussian

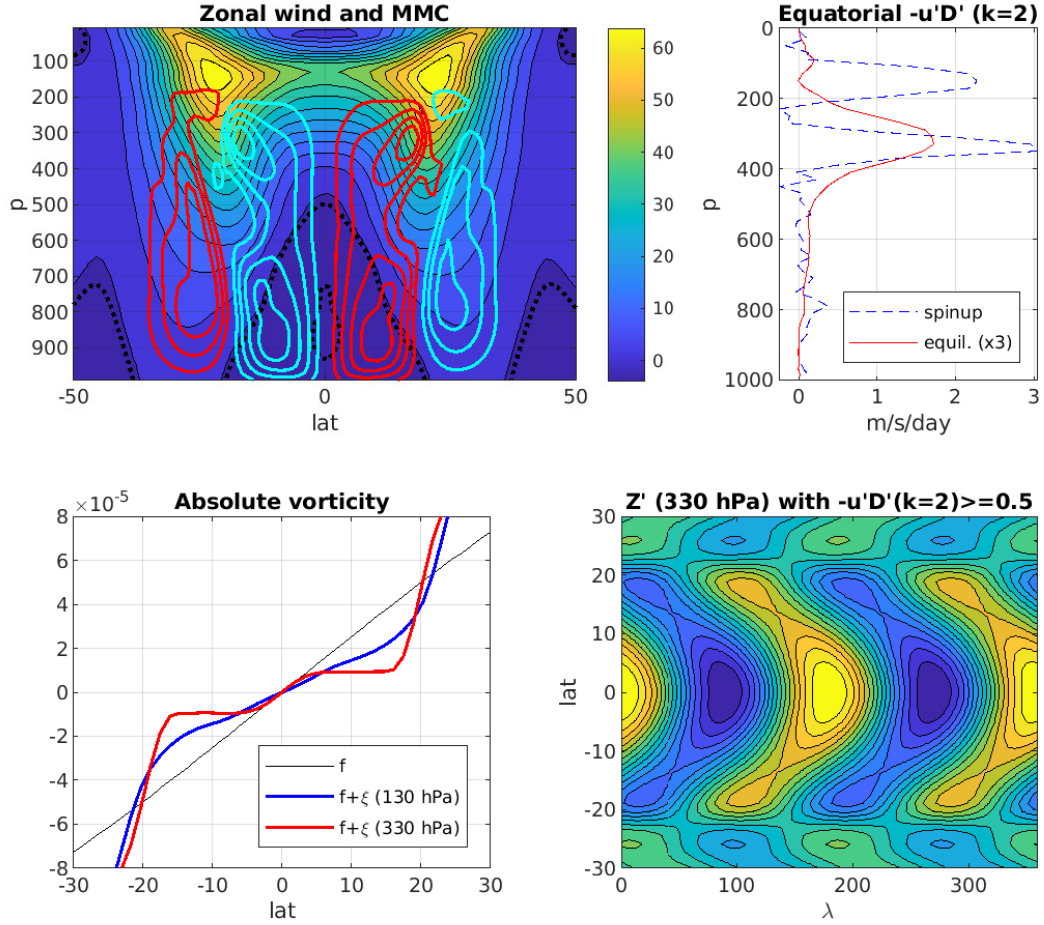


FIG. 6. (top left) Climatological zonal wind profile (shading, zero contour with thick black dotted line) and mean meridional circulation (red and cyan contours). (top right) Vertical profiles of the $k = 2$ eddy momentum flux convergence $-\overline{u'D'}$ averaged during the spinup (days 120-130, blue dashed) and in the equilibrated state (red, multiplied by 3). (bottom left) Absolute vorticity profiles at the 130 (blue) and 330 (red) hPa levels, compared to f (black). (bottom right) Composite of 330 hPa geopotential anomalies for events of large $k = 2$ equatorial acceleration.

formulation of section 2, which allows us to change the baroclinicity smoothly. The controlling parameter in this case is the Gaussian halfwidth d (Fig. 1).

Fig. 7 (top) shows the equilibrium 150 hPa zonal wind profile for values of d ranging from 10 to 40 degrees. As with the previous setup, we find a transition from earthlike (dashed) to superrotating

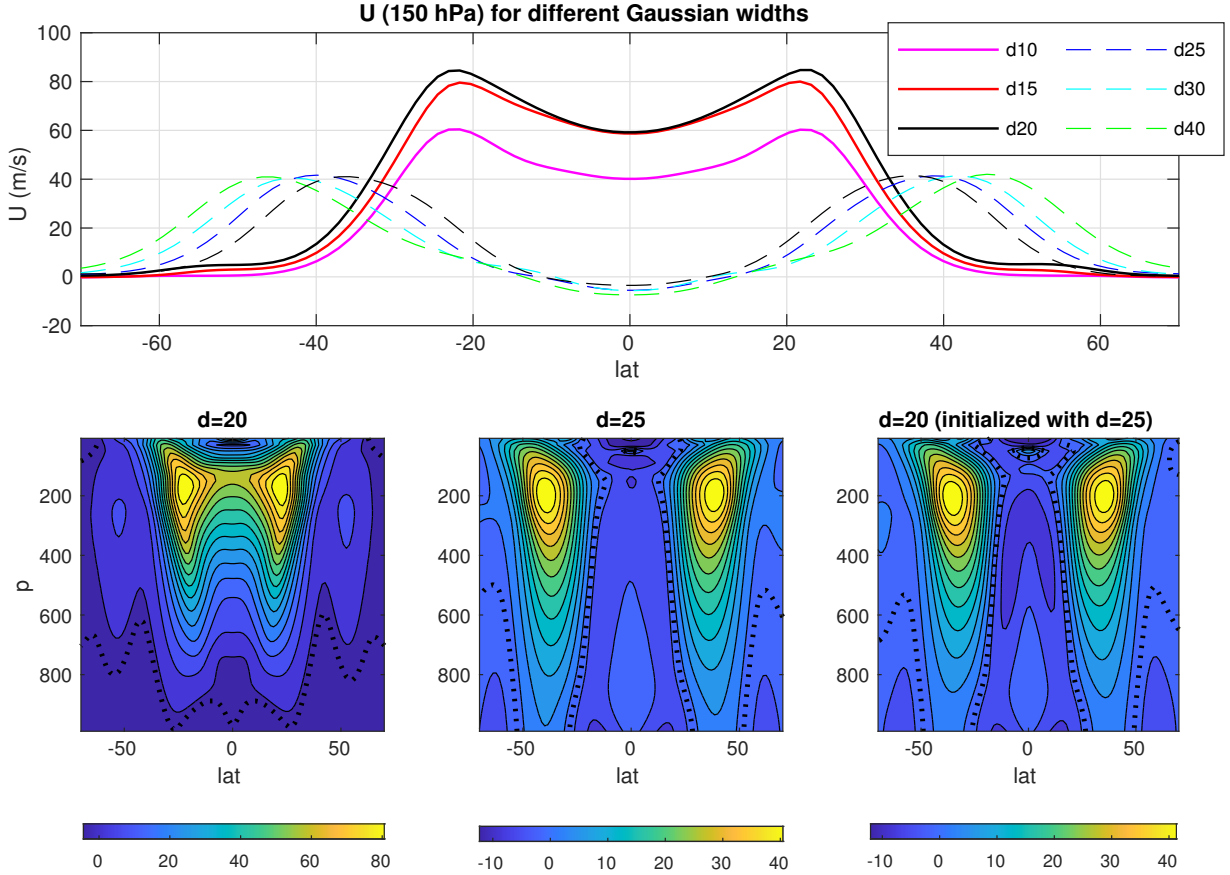


FIG. 7. (top) Equilibrated zonal wind profiles at 150 hPa for simulations using the Gaussian forcing with the widths indicated. (bottom) Full equilibrated wind profiles for: (left) $d = 20$, (center) $d = 25$, and (right) $d = 20$ initialized using the $d = 25$ simulation. In all panels, the thick black dotted line shows the zero wind contour.

(solid) climates as d decreases and the baroclinic zone moves towards the equator. The transition occurs between $d = 20$ and $d = 25$ degrees. The lower panels of Fig. 7 show the full wind structure for these two values of d . Superrotating climates have a strong subtropical jet, while earthlike climates have a much weaker extratropical jet (note the different scale in the bottom panels of Fig. 7) and weak tropical easterlies.

The transition is abrupt in that depending on the value of d , the simulation equilibrates in one or the other regime, with no intermediate states. Additionally, the system exhibits hysteresis: the $d = 20$ solution, which is superrotating when spun up from rest (black solid), persists in an earthlike regime when initialized using the equilibrated $d = 25$ simulation (black dashed). More generally, there seems to exist some sensitivity to the initial conditions around the transition region,

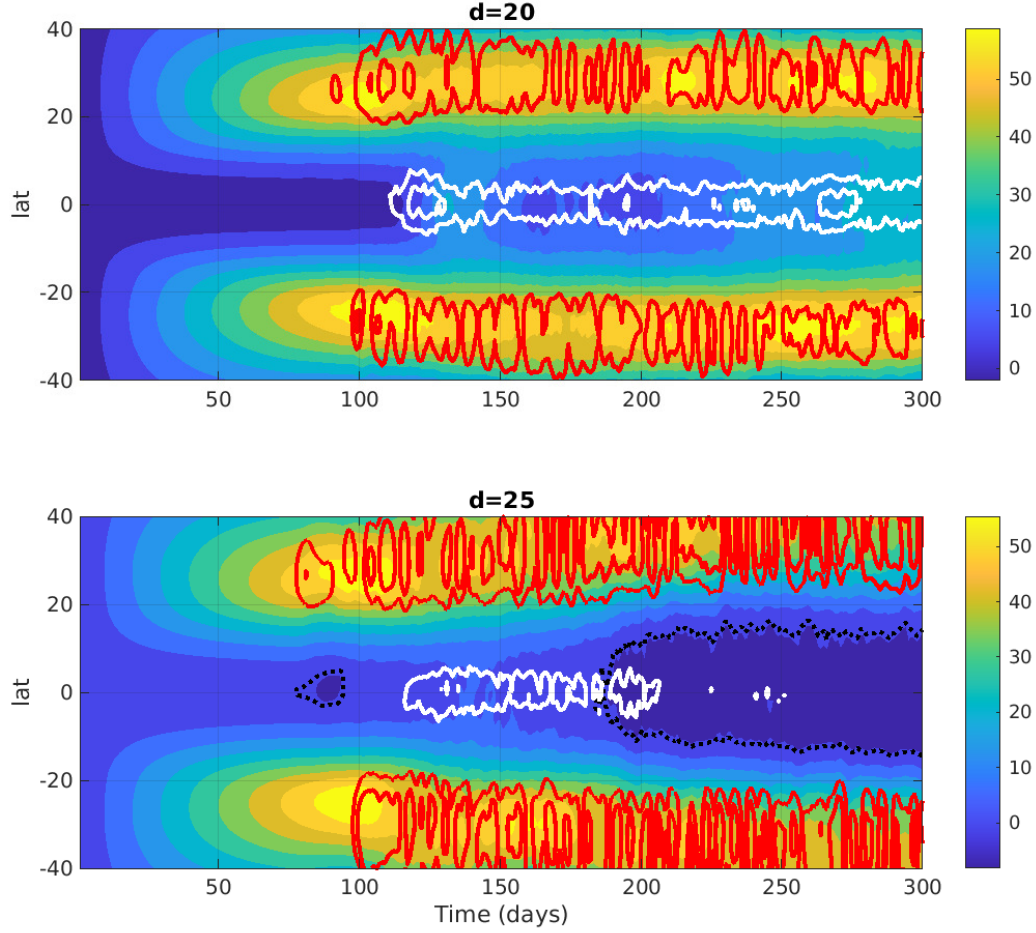


FIG. 8. Time series of 150 hPa zonal wind (shading), vertically-integrated eddy heat flux (red contours at 5 and 10 mK/s) and vertically-integrated near-equatorial $-\overline{u'D'}$ (white contours at 0.3 and 0.6 $\text{ms}^{-1}/\text{day}$) for (top) the $d = 20$ simulation and (bottom) the $d = 25$ simulation. The zero wind line is black dotted.

as expected in a chaotic system with two underlying basins of attraction. Additional simulations with $d = 16, 17$ and 19 degrees were all found to superrotate, while a simulation with $d = 18$ did not (not shown).

While we expect K-R instability to weaken when Rossby waves move poleward, the abrupt transition suggests that this does not occur smoothly as d is changed. Fig. 8 compares the upper-level wind (shading), vertically-integrated eddy heat flux (red contours) and near-equatorial

($|\phi| \leq 10$) $-\overline{u'D'}$ (white contours) for the $d = 20$ and $d = 25$ simulations during their initial spinup. We can see that K-R instability is active in both simulations (albeit weaker in the $d = 25$ case) and imparts a westerly acceleration after the subtropical jet builds up. The main difference is that while for $d = 20$ the baroclinic generation occurs at the latitude of the subtropical jet, which does not weaken or move much, for $d = 25$ the baroclinic generation occurs poleward of the subtropical jet. The baroclinic generation is also stronger in the latter case. As a result, the jet decelerates and shifts poleward in contrast with the $d = 20$ simulation.

This suggests that the key factor behind the transition from earthlike to superrotating climates is the amount of *extratropical* baroclinicity forcing. With $d \leq 20$, differential heating is confined within the tropics. As a result, changes in d only affect the Hadley cell driving but there is never substantial extratropical eddy generation. In all superrotating simulations the maximum baroclinicity and eddy heat flux are found at the edge of the Hadley cell, which remains at roughly the same latitude as d is varied (solid lines in Fig. 7). When baroclinic instability occurs at the location of the subtropical jet, it cannot easily decelerate it. It is only when the baroclinic generation occurs outside the Hadley cell that the associated eddy momentum fluxes weaken and shift the jet poleward. As this reduces the spatial overlapping between the Kelvin and Rossby waves and decreases the angular phase speed¹ of the latter, the two waves can no longer resonate and Kelvin-Rossby instability shuts down, bringing the equatorial acceleration to a halt. This also explains why superrotation does not occur for values of d near the transition when extratropical eddies are initially present.

Beyond the spinup, the two simulations also feature very different tropical-extratropical interactions in equilibrium (Fig. 9). The $d = 25$ simulation (right) is earthlike, with eddy generation and a well-defined Ferrel cell in the extratropics. In contrast, with $d = 20$ (left) the eddy generation intrudes into the Hadley-cell domain and reverses the mean meridional circulation in the subtropics. With no eddy generation in the midlatitudes, the extratropical overturning circulation is very weak, consisting of a single direct cell driven by the dissipation of the eddies generated in the subtropics (eddy momentum flux divergence not shown).

To test the idea that it is the extratropical baroclinic eddies that prevent superrotation for large d , we have devised a set of simulations in which baroclinic instability is artificially suppressed by means

¹Angular velocity, which scales as $U/\cos\phi$, decreases in these simulations because changes in jet speed are more important than changes in the radius of rotation.

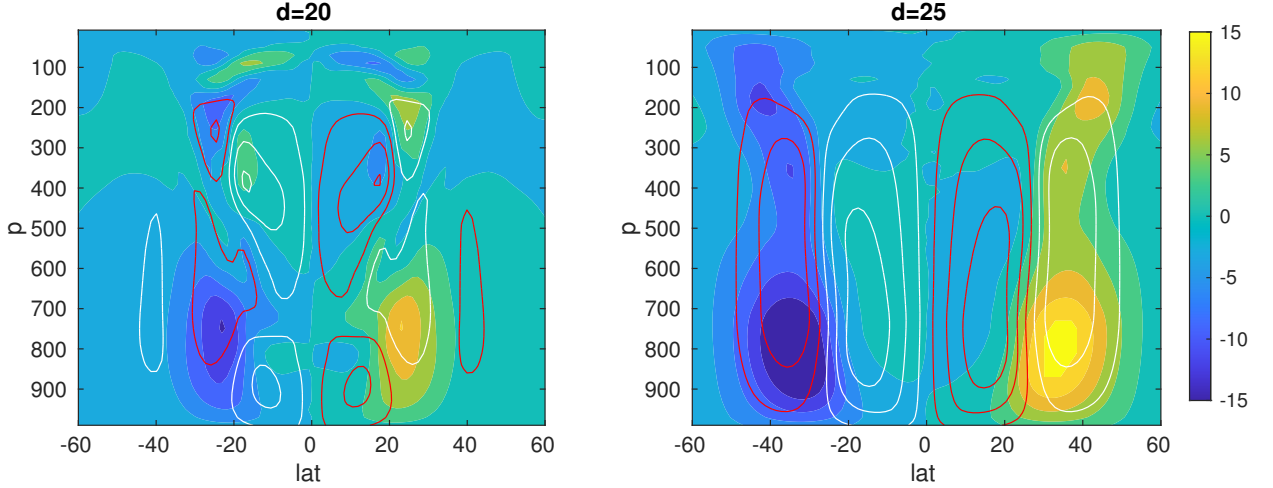


FIG. 9. Equilibrated eddy heat flux (shading) and meridional mass overturning (red and white contours at $\pm 1, 3, 5 \times 10^{10} \text{ kg/s}$) for (left) the $d = 20$ simulation and (right) the $d = 25$ simulation.

of strong diabatic eddy damping following the methods of Zurita-Gotor (2008). We accelerate the eddy diabatic timescale by a factor of 200 poleward of 40 degrees (so that tropical eddies are unaffected) while keeping the zonal-mean diabatic forcing unchanged. With this modification, the model produces superrotation for all values of d . Fig. 10 shows results for $d = 40$, the largest value considered. We can see that as extratropical eddies weaken, the subtropical jet remains strong and the maximum zonal wind is still found at the Hadley cell edge rather than at the location of maximum radiative-equilibrium baroclinicity. This provides conditions favorable for the development of Kelvin-Rossby instability, which is consistent with the structure of the perturbations driving the equatorial acceleration (the right panels of Fig. 10 show this structure for two instances of strong eddy acceleration). Other authors have also found superrotation in a terrestrial setting with reduced radiative-equilibrium temperature gradient and weakened baroclinic eddies (Laraia and Schneider 2015; Polichtchouk and Cho 2016).

5. Concluding remarks

Our results add to the growing body of literature pointing to Kelvin-Rossby instability as a viable mechanism to drive superrotation in planetary atmospheres with zonally symmetric climates. Several previous studies (Mitchell and Vallis 2010; Potter et al. 2014; Dias Pinto and Mitchell 2014) had shown this for small and/or slowly rotating planets, making this mechanism a plausible

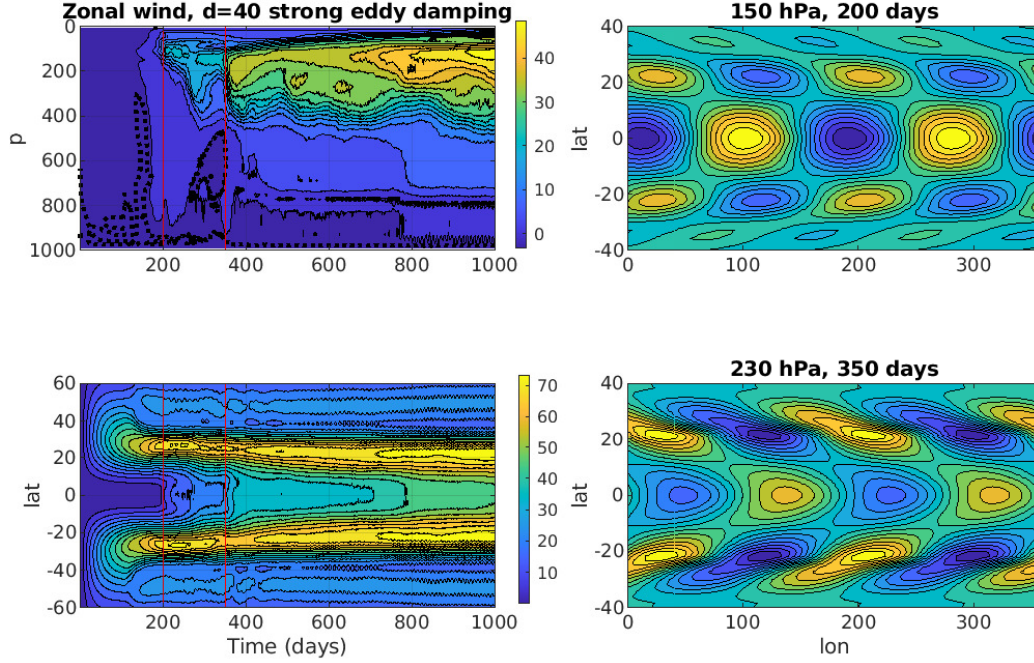


FIG. 10. (left) Time series of zonal-mean zonal wind on the equatorial plane (top, zero-wind line thick dotted) and at the 150 hPa level (bottom) for a simulation with $d = 40$ and strong extratropical eddy diabatic damping. (right) $k = 2$ geopotential anomaly at 150 hPa for $t = 200$ days (left) and at 230 hPa for $t = 350$ days, levels and times of peak eddy acceleration (cf. red lines in left panels) by these waves.

candidate to explain the superrotation of Venus and Titan. We have shown here that Kelvin-Rossby instability can also spin up superrotation with terrestrial parameters under the appropriate forcing, explaining previous results by Williams (2003).

When the baroclinic forcing is close to the equator, the spinup of superrotation is consistent with the two-step process envisioned by Gierasch (1975). Initially, the Hadley cell exports high equatorial angular momentum to the subtropics, producing a strong subtropical jet and large horizontal shear. Hydrodynamic instability then ensues and reduces this shear by transporting momentum from the jet to the equator. We have shown that the instability responsible for this transport is ageostrophic and divergent, and shares many common features with Kelvin-Rossby instability (Iga

313 and Matsuda 2005; Wang and Mitchell 2014). A linear stability analysis further demonstrates that
314 this model supports Kelvin-Rossby instability when the circulation is nearly angular-momentum-
315 conserving and the subtropical jet is strong, as found in the absence of extratropical eddies.

316 As the baroclinic forcing moves towards the midlatitudes, there is an abrupt transition in parameter
317 space to a different, more earthlike, regime, in which the jet is extratropical and eddy-driven instead
318 of subtropical, and tropical winds are easterly. We argue that the transition occurs when there is
319 enough extratropical baroclinicity to drive substantial eddy generation in the extratropics. As
320 baroclinic eddies decelerate the subtropical jet and extratropical Rossby waves slow down, they
321 cannot phase-lock with the equatorial Kelvin wave and the instability shuts down.

322 While the notion that the extratropical eddy drag prevents superrotation is not new (Saravanan
323 1993; Laraia and Schneider 2015), this hypothesis was originally motivated by the idea that the
324 easterly drag competes against some other mechanism trying to accelerate the equator, usually
325 tropical heating (e.g. Laraia and Schneider 2015). We have shown that when the equatorial accel-
326 eration is due to Kelvin-Rossby instability, the extratropical drag also works against superrotation
327 by shutting down the equatorial acceleration. This dual role may help explain the abruptness of
328 the circulation changes in our model when changing d . Baroclinic feedbacks may also play a role:
329 when the extratropical eddies are strong enough to decelerate the subtropical jet, the associated
330 eddy momentum fluxes also push the extratropical eddy generation poleward from the forcing.

331 Our analysis also helps explain the findings of Laraia and Schneider (2015) that increasing the
332 radiative-equilibrium temperature gradient works against superrotation in a rapidly rotating planet
333 but favors it in a slowly rotating one. In the latter case, the (midlatitude) baroclinicity forcing
334 occurs within the domain of the Hadley cell, which extends to high latitudes. Increasing this
335 forcing strengthens the Hadley cell and brings the high-latitude subtropical jet closer to conserving
336 angular momentum, favoring Kelvin-Rossby instability. In contrast, in a rapidly rotating planet
337 like Earth, increasing the midlatitude temperature gradient strengthens the baroclinic eddies and
338 extratropical eddy-driven jet and weakens the subtropical jet.

339 As expected based on the abruptness of the transition to superrotation, our model exhibits
340 hysteresis and may equilibrate into two different regimes near the transition point depending on
341 the initial conditions. The implications of multiple equilibria are discussed at length by Herbert
342 et al. (2020). Multiple equilibria as described here have been observed before in analytical and/or

343 symmetric models (Shell and Held 2004; Herbert et al. 2020) as well as in models in which zonally
344 asymmetric tropical heating, either stationary (Suarez and Duffy 1992) or propagating (Arnold
345 et al. 2012) is prescribed. To our knowledge, this is the first study finding subrotating/superrotating
346 multiple equilibria and hysteresis in a full primitive equation model with no externally prescribed
347 eddy forcing.

348 In conclusion, we have shown that Kelvin-Rossby coupling is a viable mechanism for spinning up
349 terrestrial superrotation. In the simulations presented here, this was achieved artificially by moving
350 the differential heating towards the equator following W03. More realistically, the coupling might
351 be achieved by slowing down the Kelvin wave (e.g., through convective coupling) and/or by
352 strengthening the subtropical jet. As convective coupling increases in a moister atmosphere, and
353 the extratropical stormtracks weaken and move poleward (e.g. Frierson et al. 2006) strengthening
354 the subtropical jet, both factors may have played a role for the terrestrial superrotation found by
355 Caballero and Huber (2010) in very warm climates.

356 *Acknowledgments.* This work was funded by the National Science Foundation, grant AGS-
 357 1733818. P.Z-G acknowledges funding by Santander UCM Grant PR87/19-22537 for the worksta-
 358 tion in which the simulations were performed. We thank J. Schrötle and two anonymous reviewers
 359 for suggestions that improved the manuscript.

360 *Data availability statement.* The simulations described in this paper were computed using the
 361 Isca model, which can be downloaded from <https://execlim.github.io/IscaWebsite/>. Output from
 362 these simulations is available from the corresponding author upon request.

363 APPENDIX

364 Linear stability analysis

365 The equatorial acceleration found in the W03 simulation with $n = 16$ (section 3) is consistent
 366 with Kelvin-Rossby instability. To demonstrate that the zonal-mean flow spun up in advance of
 367 the equatorial eddy acceleration is indeed unstable, we have performed a linear stability analysis.
 368 This can be done in the spectral model by: (i) starting from a zonal initial state, except for a
 369 small perturbation added to wavenumber k ; (ii) setting to zero in the model the tendencies for all
 370 wavenumbers different from k ; and (iii) renormalizing periodically the k spectral components for
 371 all variables whenever the amplitude of the wave exceeds some threshold (if there is instability). We
 372 set all dissipative terms to zero and construct the initial state using the hemispherically-symmetric,
 373 zonal-mean flow at $t = 115 \text{ days}$, with \bar{v} set to zero. At this time, the upper-level flow is very nearly
 374 angular-momentum-conserving as discussed in section 3.

381 The top left panel of Fig. A1 shows the dispersion relation. Maximum growth rates are found
 382 at $k = 6, 7$, with the instability tapering off for larger and smaller wavenumbers. Additionally, a
 383 second, broad peak is found at small wavenumbers, with little hint of scale selection. The two
 384 peaks grow through different mechanisms, as indicated by the dimensionless ratio:

$$385 \quad r = \frac{-\left\langle \overline{u'_k D'_k} \right\rangle \Big|_{EQ}}{\max_{\phi} \left\{ \frac{f_0}{\Delta\Theta} \left\langle \overline{v'_k T'_k} \right\rangle \right\}} \quad (\text{A1})$$

386 where the angle brackets indicate vertical integrals, $f_0 = 10^{-4} \text{ s}^{-1}$ and $\Delta\Theta = 50K$. The numerator
 387 is evaluated at the equator and the denominator at its latitudinal maximum. These two terms

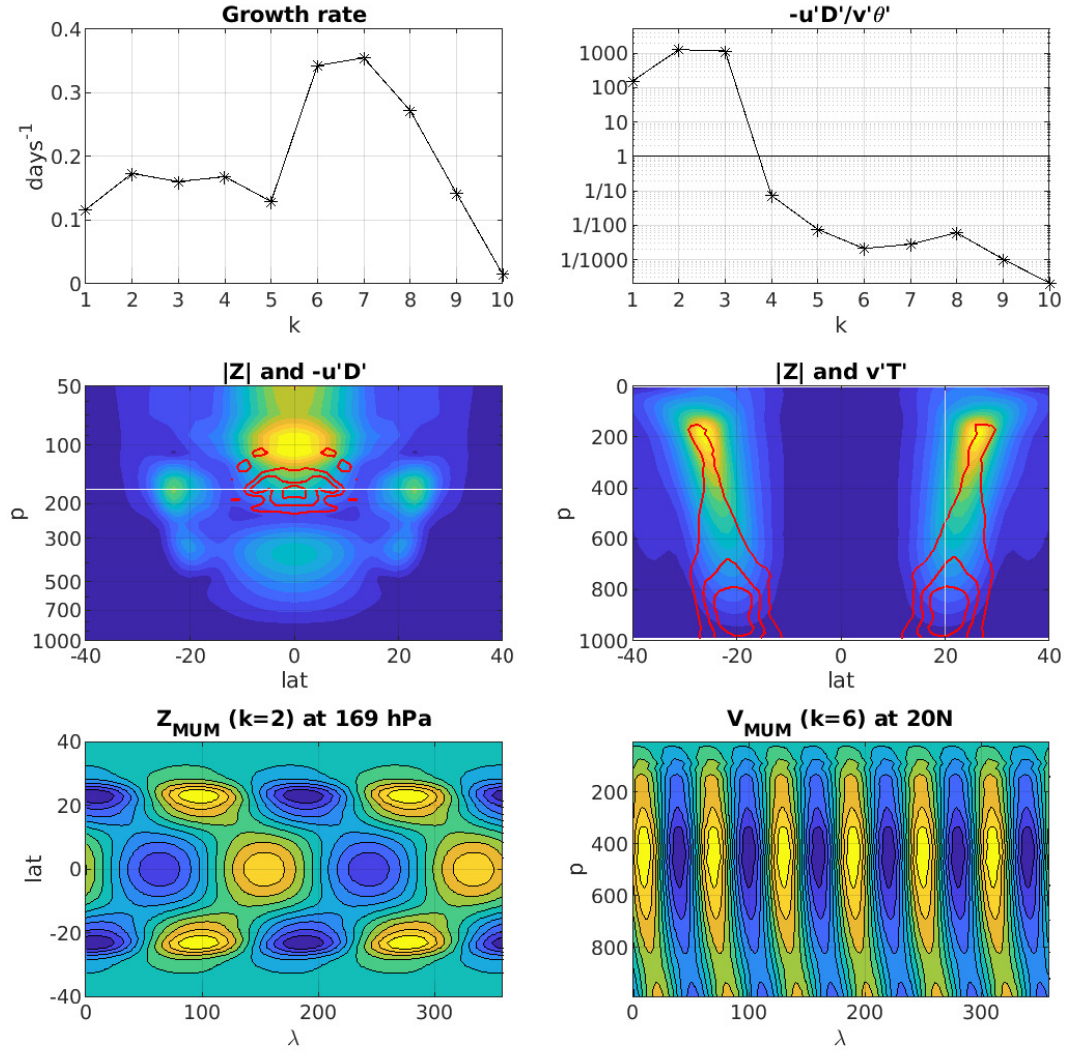


FIG. A1. (top left) Dispersion relation. (top right) Ratio between the EP divergence due to Kelvin-Rossby coupling and baroclinic processes (see text for details). (middle left) Structure of the $k = 2$ mode: eddy geopotential amplitude (shading) and positive equatorial $-\overline{u'D'}$ (red contours). (middle right) Structure of the $k = 6$ mode: eddy geopotential amplitude (shading) and eddy heat flux (red contours). (bottom left) Longitude-latitude structure of the $k = 2$ mode at the level of maximum $-\overline{u'D'}$. (bottom right) Longitude-pressure structure of the $k = 6$ mode at the latitude of maximum eddy heat flux.

may be taken as rough estimates of the Eliassen-Palm divergence due to Kelvin-Rossby instability and baroclinic instability, respectively. Fig. A1 (top right) shows that $r \gg 1$ for $k = 1 - 3$ and $r \ll 1$ for $k \geq 5$, suggesting that the former (latter) waves grow through Kelvin-Rossby (baroclinic) instability.

This is also consistent with the structure of the modes, shown in the bottom two rows of Fig. A1 for $k = 2$ (left) and $k = 6$ (right). The $k = 2$ mode has maximum amplitude in the subtropical upper troposphere and over the equatorial plane, and produces an acceleration ($-\overline{u'D'}$, red contours) in the equatorial upper troposphere. The $k = 6$ mode has a single maximum over the jet and lower-troposphere eddy heat flux (red contours) slightly equatorward of it. Finally, the longitude-latitude structure of the $k = 2$ mode at the level of peak $-\overline{u'D'}$ and the longitude-pressure structure of the $k = 6$ mode at the latitude of maximum eddy heat flux have the required phase tilts.

The $k = 2$ most unstable mode displays many similarities with the the structure of the perturbation described in section 3, but also some differences. This may be due to nonlinearity or it may reflect nonmodal behavior in the full-model evolution.

References

- Arnold, N. P., E. Tziperman, and B. Farrell, 2012: Abrupt transition to strong superrotation driven by equatorial wave resonance in an idealized GCM. *Journal of the Atmospheric Sciences*, **69** (2), 626–640.
- Caballero, R., and M. Huber, 2010: Spontaneous transition to superrotation in warm climates simulated by CAM3. *Geophys. Res. Lett.*, **37** (11).
- Dias Pinto, J. R., and J. L. Mitchell, 2014: Atmospheric superrotation in an idealized GCM: Parameter dependence of the eddy response. *Icarus*, **238**, 93–109.
- Frierson, D. M., I. M. Held, and P. Zurita-Gotor, 2006: A gray-radiation aquaplanet moist GCM. Part I: Static stability and eddy scale. *Journal of the atmospheric sciences*, **63** (10), 2548–2566.
- Gierasch, P. J., 1975: Meridional circulation and the maintenance of the Venus atmospheric rotation. *Journal of Atmospheric Sciences*, **32** (6), 1038–1044.

- 414 Held, I. M., and M. J. Suarez, 1994: A proposal for the intercomparison of the dynamical cores
415 of atmospheric general circulation models. *Bulletin of the American Meteorological society*,
416 **75 (10)**, 1825–1830.
- 417 Herbert, C., R. Caballero, and F. Bouchet, 2020: Atmospheric bistability and abrupt transitions to
418 superrotation: wave–jet resonance and Hadley cell feedbacks. *Journal of Atmospheric Sciences*,
419 **77 (1)**, 31–49.
- 420 Hide, R., 1969: Dynamics of the atmospheres of the major planets with an appendix on the viscous
421 boundary layer at the rigid bounding surface of an electrically-conducting rotating fluid in the
422 presence of a magnetic field. *J. Atmos. Sci.*, **26 (5)**, 841–853.
- 423 Iga, S.-I., and Y. Matsuda, 2005: Shear instability in a shallow water model with implications for
424 the Venus atmosphere. *J. Atmos. Sci.*, **62 (7)**, 2514–2527.
- 425 Laraia, A. L., and T. Schneider, 2015: Superrotation in terrestrial atmospheres. *Journal of the*
426 *Atmospheric Sciences*, **72 (11)**, 4281–4296.
- 427 Mendonça, J. M., and P. L. Read, 2016: Exploring the Venus global super-rotation using a
428 comprehensive general circulation model. *Planetary and space science*, **134**, 1–18.
- 429 Merlis, T. M., and T. Schneider, 2010: Atmospheric dynamics of earth-like tidally locked aqua-
430 planets. *Journal of Advances in Modeling Earth Systems*, **2 (4)**.
- 431 Mitchell, J. L., and G. K. Vallis, 2010: The transition to superrotation in terrestrial atmospheres.
432 *Journal of Geophysical Research: Planets*, **115 (E12)**.
- 433 Polichtchouk, I., and J. Cho, 2016: Equatorial superrotation in Held and Suarez like flows with
434 weak equator-to-pole surface temperature gradient. *Quart. J. Roy. Meteor. Soc.*, **142 (696)**,
435 1528–1540.
- 436 Potter, S. F., G. K. Vallis, and J. L. Michell, 2014: Spontaneous superrotation and the role of
437 Kelvin waves in an idealized dry GCM. *J. Atmos. Sci.*, **71 (2)**, 596–614.
- 438 Read, P. L., and S. Lebonnois, 2018: Superrotation on Venus, on Titan, and elsewhere. *Annual*
439 *Review of Earth and Planetary Sciences*, **46**, 175–202.

440 Saravanan, R., 1993: Equatorial superrotation and maintenance of the general circulation in two-
441 level models. *J. Atmos. Sci.*, **50** (9), 1211–1227.

442 Schneider, T., and J. Liu, 2009: Formation of jets and equatorial superrotation on Jupiter. *Journal*
443 *of the atmospheric sciences*, **66** (3), 579–601.

444 Shell, K. M., and I. M. Held, 2004: Abrupt transition to strong superrotation in an axisymmetric
445 model of the upper troposphere. *J. Atmos. Sci.*, **61** (23), 2928–2935.

446 Showman, A. P., and L. M. Polvani, 2011: Equatorial superrotation on tidally locked exoplanets.
447 *The Astrophysical Journal*, **738** (1), 71.

448 Suarez, M. J., and D. G. Duffy, 1992: Terrestrial superrotation: A bifurcation of the general
449 circulation. *J. Atmos. Sci.*, **49** (16), 1541–1554.

450 Takagi, M., and Y. Matsuda, 2007: Effects of thermal tides on the Venus atmospheric superrotation.
451 *Journal of Geophysical Research: Atmospheres*, **112** (D9).

452 Vallis, G. K., and Coauthors, 2018: Isca, v1.0: a framework for the global modelling of the
453 atmospheres of earth and other planets at varying levels of complexity. *Geoscientific Model*
454 *Development*, **11** (3), 843–859, <https://doi.org/10.5194/gmd-11-843-2018>, URL <https://gmd.copernicus.org/articles/11/843/2018/>.

456 Wang, P., and J. L. Mitchell, 2014: Planetary ageostrophic instability leads to superrotation.
457 *Geophys. Res. Lett.*, **41** (12), 4118–4126.

458 Williams, G., 2003: Barotropic instability and equatorial superrotation. *Journal of the atmospheric*
459 *sciences*, **60** (17), 2136–2152.

460 Zurita-Gotor, P., 2008: The sensitivity of the isentropic slope in a primitive equation dry model.
461 *Journal of the atmospheric sciences*, **65** (1), 43–65.

462 Zurita-Gotor, P., 2019: The role of the divergent circulation for large-scale eddy momentum
463 transport in the tropics. Part I: Observations. *Journal of the atmospheric sciences*, **76** (4),
464 1125–1144.

- 465 Zurita-Gotor, P., and I. M. Held, 2018: The finite amplitude evolution of mixed Kelvin-Rossby
466 wave instability and equatorial superrotation in a shallow water model and an idealized GCM.
467 *Journal of the Atmospheric Sciences*, **75**, 2299–2316.
- 468 Zurita-Gotor, P., and I. M. Held, 2021: Westward-propagating Rossby modes in idealized GCMs.
469 *Journal of the Atmospheric Sciences*, **78 (5)**, 1503–1522.